AIAA SciTech Forum
8-12 January 2024, Orlando, FL
AIAA SCITECH 2024 Forum

10.2514/6.2024-2570

Improved Debris Blocker and Flow Terminator in a Shock Tunnel

B. A. Segall*, J. D. Langhorn†, and N. J. Parziale‡
Stevens Institute of Technology, Hoboken, NJ 07030, USA

T. Keenoy§ and D. Shekhtman¶
Fairfield University, Fairfield, CT 06824, USA

This paper describes an updated nozzle centerbody, which acts as both a flow terminator and a debris blocker in the Stevens Shock Tunnel. A redesigned centerbody that slides on linear bearings was implemented to reduce tunnel turn-around time, increase plugging-time control, and improve shot-to-shot consistency in the facility. Pressure traces for shock tunnel experiments using the new centerbody design are presented to demonstrate comparable behavior to the previous version. Design features are discussed, and the new centerbody design will be further evaluated in future experimental work. A preliminary computational fluid dynamics analysis is also presented to explore and describe the plugging action of the debris blocker.

I. Introduction

High-speed vehicle design requires the prediction of wall-heat flux, surface force distributions, and flow stability. Transition and turbulence studies at flight conditions are needed to validate computational fluid dynamic (CFD) codes, which are used to design vehicles. Impulse facilities, such as shock tunnels, generate hypersonic flow to replicate flight enthalpy conditions for time intervals on the order of milliseconds [1]. The testing environment inside the test section of a shock tunnel is harsh due to high temperatures, fast-moving flow debris, and mechanical vibration [2]. Observing transition mechanisms and measuring turbulence quantities (i.e. velocity fluctuations, wall shear, surface heat flux profiles) require experiments that minimize unwanted disturbances, such as diaphragm debris and tunnel vibration. Additionally, obstructing tunnel debris protects the surfaces of test articles from damage and may assist in preventing artificial flow transition. Using a nozzle centerbody in a shock tunnel can reduce debris in the test section, prevent test section over-pressure, decrease facility recoil, and allow driver gas recovery.

Researchers have employed different strategies to mitigate these concerns. Herzberg et al. [3] used a nozzle positioned at an angle away from the shock-tube axial direction, thus using centrifugal force to accelerate particulate out of the flow. Chue and Eitelberg [4] studied the shock-wave/boundary-layer interaction in the reservoir of the High Enthalpy Shock Tunnel Göttingen (HEG) facility [5]. That work focused on the flow structure around a cylindrical plate positioned near the nozzle throat that acts as a "particle stopper." Holden [6, 7] describes a method in the Large Energy National Shock Tunnel (LENS) tunnels where the flow is terminated after the test time by a "fast-acting valve" that closes the nozzle throat to protect the models and the throat from thermal or mechanical damage. Efforts have also been made to prevent dump tank over-pressurization after high-pressure tests. Lee et al. discuss a design/experimentation study of a "stationary throat plug" [8, 9] in addition to a "moving throat plug" [10] in the Korea Advanced Institute of Science and Technology (KAIST) shock tunnel. Hornung and Parziale [11] explored introducing a "blocker" near the nozzle throat of the T5 reflected-shock tunnel [12] to reduce particle impact on a model, as others have done, and also reduce freestream disturbances by disrupting the focusing of the radially-propagating shock wave during tunnel startup. Shekhtman and Segall et al. [13, 14] implemented a debris blocker and flow terminator consisting of a neoprene ball suspended in the flow in the nozzle reservoir. The work demonstrated the ability of a ball centerbody to block particles in shock-tunnel-generated flow, prevent dump tank pressurization, and plug the flow after the desired test time to allow for driver gas reclamation, without introducing disturbances in the flow. This ball centerbody was implemented by Segall et al. [15, 16] in experimentation and confirmed its ability to protect test articles and prevent dump tank over-pressurization.

*Graduate Student, Mechanical Engineering, Castle Point on Hudson, Hoboken, New Jersey, 07030.
†Graduate Student, Mechanical Engineering, Castle Point on Hudson, Hoboken, New Jersey, 07030.
‡Associate Professor, Mechanical Engineering, Castle Point on Hudson, Hoboken, New Jersey, 07030, AIAA Associate Fellow.
§Graduate Student, Mechanical Engineering, 1073 North Benson Road, Fairfield, Connecticut, 06824
¶Assistant Professor, Mechanical Engineering, 1073 North Benson Road, Fairfield, Connecticut, 06824

This paper follows up on our AIAA Journal Technical Note [14] and introduces an updated centerbody design. This updated model offers better performance than the previously used suspended neoprene ball in key areas such as shot-to-shot consistency/reliability and improved closing characteristics. Design considerations are discussed and pressure traces are presented to demonstrate the performance and features of the centerbody.

II. Experimental Setup

A. Ground-Test Facility Facility

The Stevens Shock Tunnel (SST) is a facility designed to replicate Mach 6 free-flight flow conditions with an enthalpy of 1.5 MJ/kg and a unit Reynolds number 0.35 - 8.1 $\times 10^6$ m^{-1} for at least 5 ms when using helium as a driver gas. The construction of the shock tunnel adheres to ASME standard B16.5 Pipe Flanges and Flanged Fittings for flanges and olets [17] and ASME standard B31.1 Power Piping for all pipes [18]. In Fig. 1, the current configuration of the tunnel is displayed. The driver section is 5.0 m long, and the driven section is 11.07 m long. A double diaphragm is used to start the tunnel. Up to 5 transducer stations are used to provide a shock-speed measurement. The test section has an inner diameter of 0.610 m (24 in) and is large enough to accommodate a 34° hollow-cylinder flare of 0.102 m (4 in) outer cylinder diameter and 0.203 m (8 in) outer flare diameter without tunnel startup issues. A Pitot pressure probe is located at the nozzle exit to determine freestream conditions during each run, via the Rayleigh-Pitot tube relation and the assumption of isentropic nozzle flow [19, 20]. Further mechanical details on the Stevens Shock Tunnel can be found in Shekhtman et al. [13].

The tunnel runs were conducted with either nitrogen N_2 or helium He as the driver gas and various driven gases, such as air and krypton-doped nitrogen. Run conditions are shown in Table 1. Reservoir conditions were calculated with both Cantera and the Shock and Detonation Toolbox [21]. The appropriate thermodynamic data are found in the literature [22, 23]. Freestream conditions were calculated via the method described in Mustafa et al. [19], utilizing reservoir and Pitot pressure traces and assuming an isentropic expansion iterating to find freestream Mach number. Representative pressure traces for shots 300, 303, 306 and 391 are shown in Appendix A in Figs. 11a to 11d. Using nitrogen as the driver gas and a pressure ratio of 10, the typical enthalpy in the nozzle reservoir is 0.5 MJ/kg with a test time of 10-14 ms, limited by the arrival of a compression wave, which is generated by the reflection of the reflected shock at the contact surface. This is in contrast with 5 ms test times achieved with a helium driver, which is limited by the arrival of the expansion wave. With the use of a diaphragm debris blocker, as described in Shekhtman et al. [13], the Pitot traces exhibit small oscillation and demonstrate the establishment of steady flow during test times indicated by a heavy red line weight.

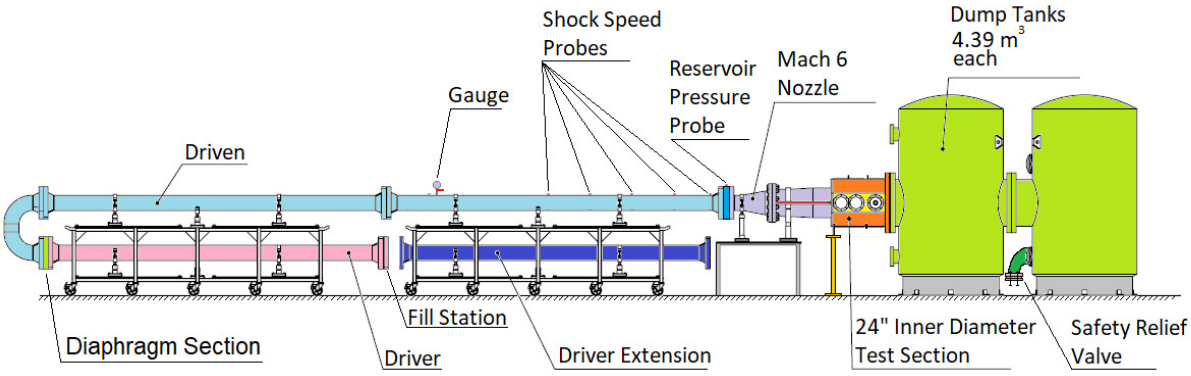

Fig. 1 Schematic of Stevens Shock Tunnel. For scale, the single section of driver tube is 5 m.

B. Nozzle Centerbody

A nozzle centerbody was installed in the nozzle reservoir region of the Stevens Shock Tunnel. The centerbody is shown in Fig. 2a with individual parts labeled in Fig. 2b. Unlike the previous iteration of the centerbody which consisted of a suspended neoprene ball that swung into the nozzle converging section, the new centerbody is constrained to slide linearly toward the nozzle throat. As shown in Fig. 2b, the centerbody assembly consists of a solid neoprene

Table 1 Run Conditions, where P_4 is the driver-section gas pressure; P_4/P_1 is the driver-to-driven pressure ratio that determines the driven gas pressure P_1; u_s is the shock speed; M_s is the shock Mach number; T_r is the reservoir temperature; P_r is the reservoir pressure; P_∞ is the freestream pressure, T_∞ is the freestream temperature, M_∞ is the freestream Mach number, V_∞ is the freestream velocity, and Re^u_∞ is the unit Reynolds number. Freestream pressure, temperature, velocity, and Reynolds number are calculated nozzle pitot tube and nozzle reservoir pressures, using the method described in Mustafa et al. [19], assuming an isotropic nozzle with chemical reactions. The centerbody column designates the type of nozzle centerbody.

Shot	P_4 (MPa)	$\frac{P_4}{P_1}$	Driver Gas	Test Gas	u_s (m/s)	M_s	P_R (MPa)	T_r (K)	P_∞ (kPa)	T_∞ (K)	M_∞	V_∞ (m/s)	Re^u_∞ (10^6 1/m)	Center-body
184	7.03	111	He	Air	1195	3.44	5.16	1600	3.18	230	5.84	1779	5.88	Ball
185	8.26	110	He	Air	1219	3.51	6.11	1659	3.68	233	5.85	1797	6.68	Ball
186	3.55	110	He	Air	1195	3.44	2.60	1627	1.65	231	5.82	1776	3.00	Ball
283	1.76	10	N_2	1% Kr-99% N_2	513	1.47	1.09	518	0.66	62.8	6.04	962	8.52	Ball
289	3.44	10	N_2	Air	514	1.53	2.12	516	1.29	62.8	6.03	959	16.7	Ball
300	3.45	10	N_2	Air	533	1.53	2.12	521	1.12	63.2	6.23	967	14.4	Slider
303	3.46	10	N_2	5% Kr-95% N_2	526	1.56	2.17	533	1.14	65.7	6.29	942	14.0	Slider
306	1.76	10	N_2	3% Kr-97% N_2	531	1.55	1.09	528	0.60	66.5	6.23	956	6.97	Slider
365	7.58	117	He	5% Kr-95% N_2	1224	3.63	5.54	1795	3.45	244	5.88	1792	6.15	Slider
366	7.58	117	He	5% Kr-95% N_2	1234	3.65	5.48	1804	3.14	240	5.96	1800	5.81	Slider
367	7.58	117	He	5% Kr-95% N_2	1230	3.63	5.47	1797	3.28	242	5.92	1800	5.97	Slider
385	3.44	10	N_2	5% Kr-95% N_2	521	1.54	2.19	532	1.11	65.3	6.31	942	13.9	Slider
391	7.58	117	He	5% Kr-95% N_2	1229	3.60	5.53	1801	3.06	237	6.00	1800	5.79	Slider

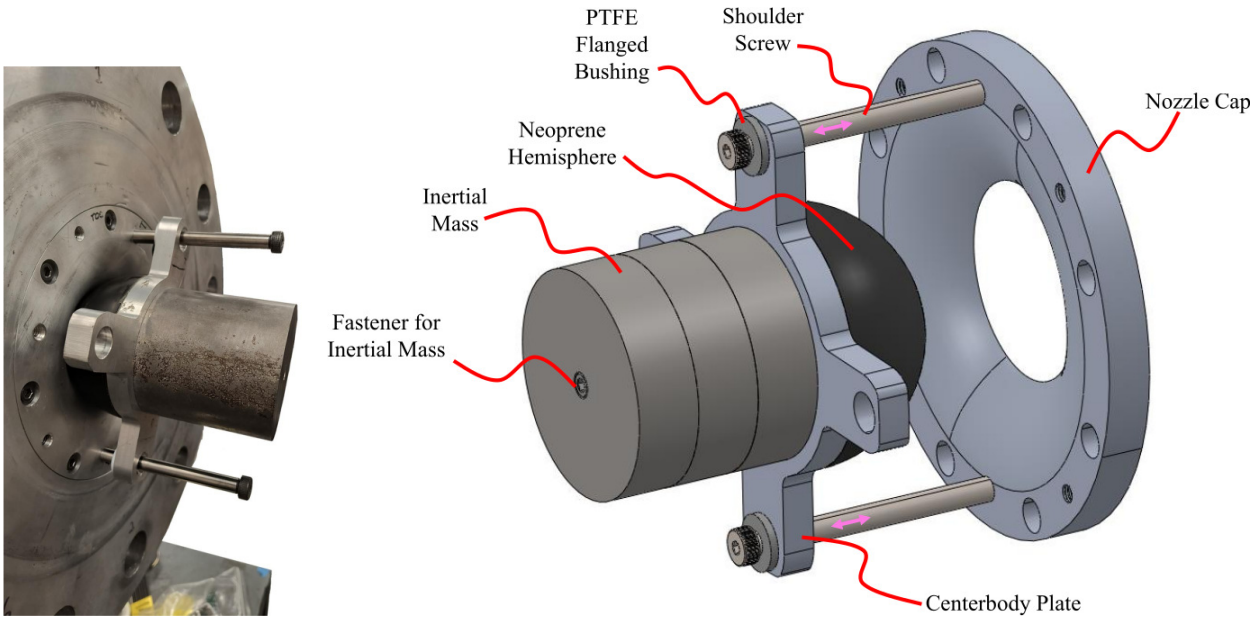

(a) Centerbody in the SST **(b) Centerbody Assembly**

Fig. 2 Nozzle Centerbody: (a) Design and (b) Implementation.

hemisphere mounted onto an aluminum plate with PTFE flanged bushings that slide along two 3/8-in diameter shoulder screws. The shoulder screws are screwed into a nozzle throat cap which clamps the secondary diaphragm in place. The neoprene half-ball functions as a plug for the nozzle. In the rear of the aluminum plate, an adjustable inertial mass is used to tune the closing time of the centerbody. The new design offers several advantages: (1) the shoulder screw design ensures the centerbody centered throughout the run; (2) mounting the centerbody to the nozzle throat cap enables quick turnaround time; (3) centerbody sealing time is adjustable and tunable; (4) concept is more structurally robust; and (5)

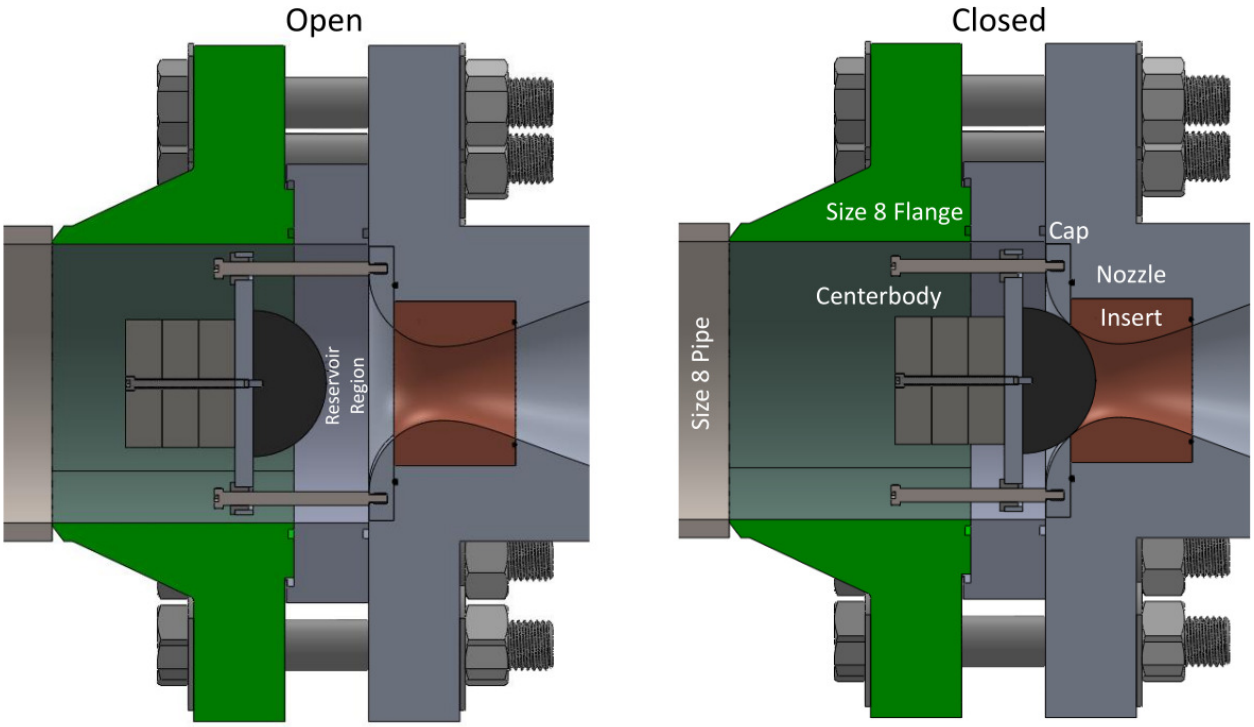

Fig. 3 Side View of Centerbody Plugging the Nozzle.

the neoprene hemisphere is less prone to bouncing off the nozzle surface due to its increased inertia. In Fig. 2a, the centerbody prototype is shown in its closed state in the nozzle reservoir region of the Stevens Shock Tunnel. Side-view schematics of the open and closed states of the sliding-plug centerbody are presented in Fig. 3. During an experiment, the centerbody obtains initial momentum relative to the shock tube from both the facility recoil and the incident shock wave to translate downstream towards the nozzle converging section. The inertia of the centerbody is set such that the centerbody reaches the surface of the nozzle after the useful test time of the facility. Using Fig. 4, the closing time of the centerbody is estimated to be

$$t_{close} = \frac{\left[\Delta x - u_t \left(\frac{L_{\text{Driven}}}{u_s}\right)\right]}{\left(\frac{P_2 A}{u_s}\right)\left(\frac{r_{\text{ball}}+t_{\text{plate}}+L_{\text{mass}}}{m_{\text{ball}}+m_{\text{plate}}+\rho_{\text{steel}} A_{\text{mass}} L_{\text{mass}}}\right)}. \tag{1}$$

The numerator of the Eq. 1 represents the remaining stroke ($< \Delta x$) of the centerbody after the tunnel has recoiled at velocity $u_t = (m_{\text{Driven,gas}} + m_{\text{Driver,gas}})u_2/m_{\text{tunnel,pipes}}$ during the time it takes for the incident shock to arrive L_{Driven}/u_s at the centerbody from the diaphragm station. The denominator of Eq. 1 is the velocity of the centerbody resulting from momentum transfer from the incident shock passing over the body. Gas processed by the incident shock moving at speed u_s results in pressure P_2 and velocity u_2 relative to the tunnel. The front-facing projected area of the centerbody is A. The residence time of the shock wave on the centerbody is estimated as $(r_{\text{ball}} + t_{\text{plate}} + L_{\text{mass}})/(u_s)$. The impulse is from the shock therefore calculated as $P_2 A(r_{\text{ball}} + t_{\text{plate}} + L_{\text{mass}})/(u_s)$. Dividing the impulse by the mass of the centerbody, the velocity of the centerbody is obtained. Eq. 1 can be used to estimate the length of required inertial mass L_{mass}. Once at the surface, the centerbody forms a plug seal, terminating the nozzle flow. For nitrogen-driven shots, P_2 should be replaced with P_5. For shots 300, 303, and 306, the mass of the centerbody is 5 kg, and the estimated plugging time is ≈50 ms.

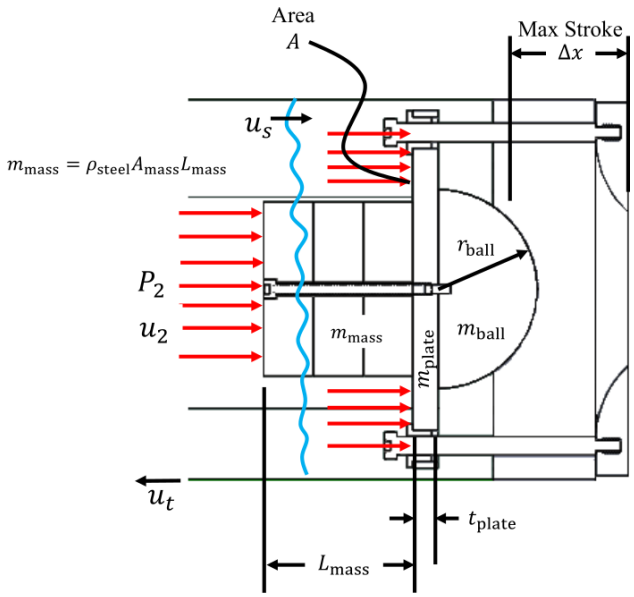

Fig. 4 Sketch of Nozzle Centerbody for Plugging Time Model.

III. Centerbody Results and Discussion

Pressure traces from testing performed in the Stevens Shock Tunnel are presented to compare the performance of the previous and updated centerbody designs. As shown in Fig. 5, the nozzle wall static pressure traces of shots listed in Table 1 depict the usable test time and plugging times of the nozzle centerbody. Smooth traces in the test time indicate clean flow which both centerbody designs achieve consistently. The centerbody plugging time is indicated by the rising edge of the right-hand pressure plateau. In Fig. 5a, it is observed that the ball centerbody closes at approximately the same time for every run when using N_2 as a driver gas. This phenomenon is concerning because shots with higher driver pressure and the same pressure ratio will increase the pressure acting on the ball centerbody, which should decrease the ball plugging time. We are currently only able to speculate on the performance of the ball centerbody. We believe that there may be cases where the ball centerbody does not immediately seat itself in the nozzle throat.

The updated sliding centerbody translates as a result of an impulse from the incident shock. Its rear inertial mass allows for customization of its mass to control the plugging time at the nozzle throat. In shots 300, 303, and 306 with the sliding centerbody, the mass of the centerbody was ≈5 kg. Shots 300 and 303 have a higher driver pressure than shot 306. The lower pressure shot, which featured a decreased driven slug pressure, took longer for the slider to plug the nozzle throat, which was expected due to decreased impulse acting on the body. An analysis was performed to obtain the weight of the inertial mass to emulate the plugging time of the original ball centerbody for the nitrogen driver gas condition. After testing various weights, it was determined that a mass of approximately 2 kg yielded almost identical run results between the two centerbodies with similar run conditions. Shots 289 and 385 in Fig. 5 show the successful replication of the plugging behavior. For helium driver experiments, the mass of the centerbody was decreased to 1 kg to have a plugging time of ≈ 20 ms as shown in Fig. 5b. The sliding centerbody plugged without bouncing off the nozzle throat and experienced consistent plugging behavior for each experiment run.

Plugging times for both the N_2 and He shots were determined using the nozzle wall static pressure traces shown in Fig. 5. These values were compared to the calculated closing time values using Eq. 1. This is shown in Fig. 6. A linear regression was performed on the data to validate linearity between the calculated and measured closing times. This yielded a slope slope of 0.94 with an R^2 value of 0.96. This shows a 1:1 correspondence between the predicted and measured closing times.

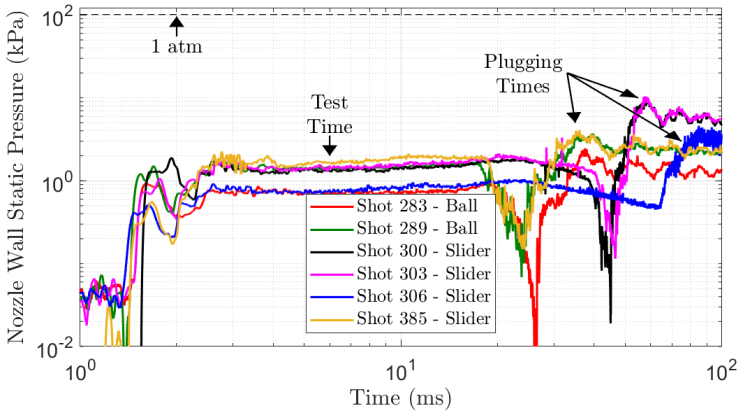

(a) N_2-Driven Shot Plugging Times

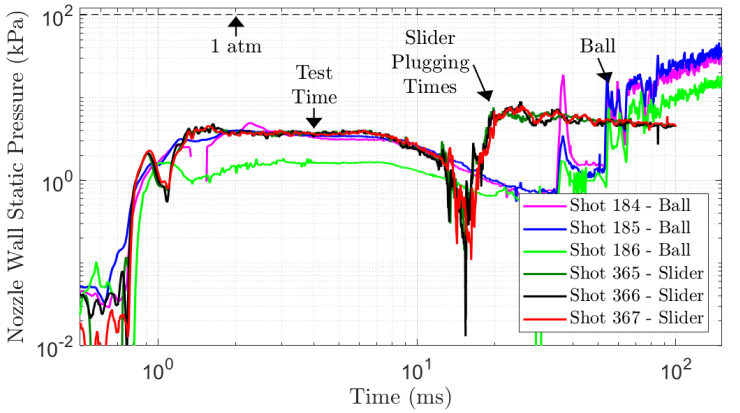

(b) He-Driven Shot Plugging Times

Fig. 5 Nozzle Wall Static Pressure Traces showing Plugging Times for Stevens Shock Tunnel using a sliding nozzle centerbody.

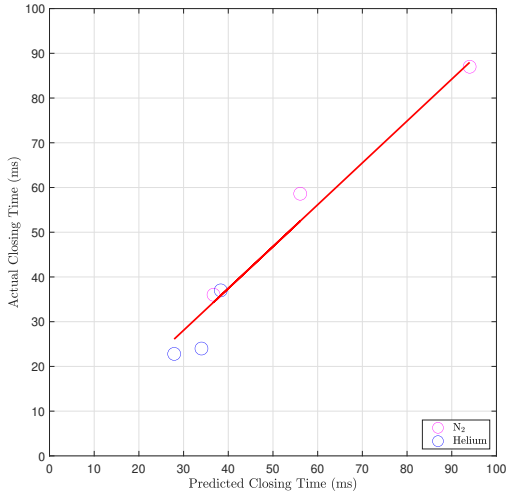

Fig. 6 Closing time comparisons between Eq. 1 and experimental closing time.

IV. Preliminary Numerical Simulation of Nozzle Centerbody

Using *ANSYS Academic Research Fluent 2023 R1*, a transient, axisymmetric compressible flow simulation was performed for a centerbody plugging converging section of the Mach 6 nozzle. The nozzle geometry is shown in Fig. 7. Unlike Hameed et al. [24], the nozzle converging section geometry has been modified with pipe extension and the inclusion of a nozzle centerbody which is depicted by a semicircle cutout in the axisymmetric geometry. The nozzle geometry was split and meshed into three sections. As shown in Fig. 8, region 1 (the leftmost portion of the converging section) was meshed with uniform 2 mm large triangular elements because ANSYS Fluent can only remesh triangular elements. The element size was set to 1 mm at the throat plane and 5 mm at the exit plane, and the bias factor toward the nozzle wall was set to 5. Region 3 (the diverging section) and region 2 (the right-most portion of the converging section nearest the throat) were meshed with quadrilateral elements that were clustered near the throat and the nozzle wall, via ANSYS's built-in biased meshing feature. The axial element size in the diverging section was 5 mm with a bias factor of 5 towards the throat. Dynamic remeshing was specified for section 1 as well as its axial boundary of this section. Rigid body, 1-degree-of-freedom motion was allowed for the wall-boundary defining the nozzle centerbody. The nozzle centerbody was assumed to have a mass of 1 kg and an initial velocity of 2 m/s, which was imparted by the impulse of the incident shock (defined by the incident shock residence time). Its leading edge was positioned approximately 80 mm from the nozzle. All other surfaces of the nozzle were designated to be stationary. The centerbody motion was permitted to move with the nozzle reservoir flow.

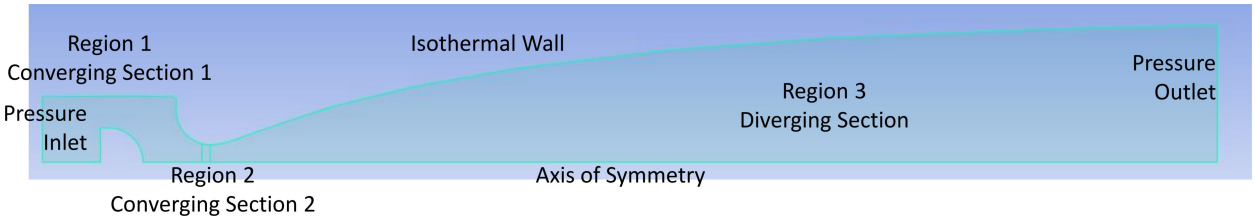

Fig. 7 Nozzle Geometry Setup.

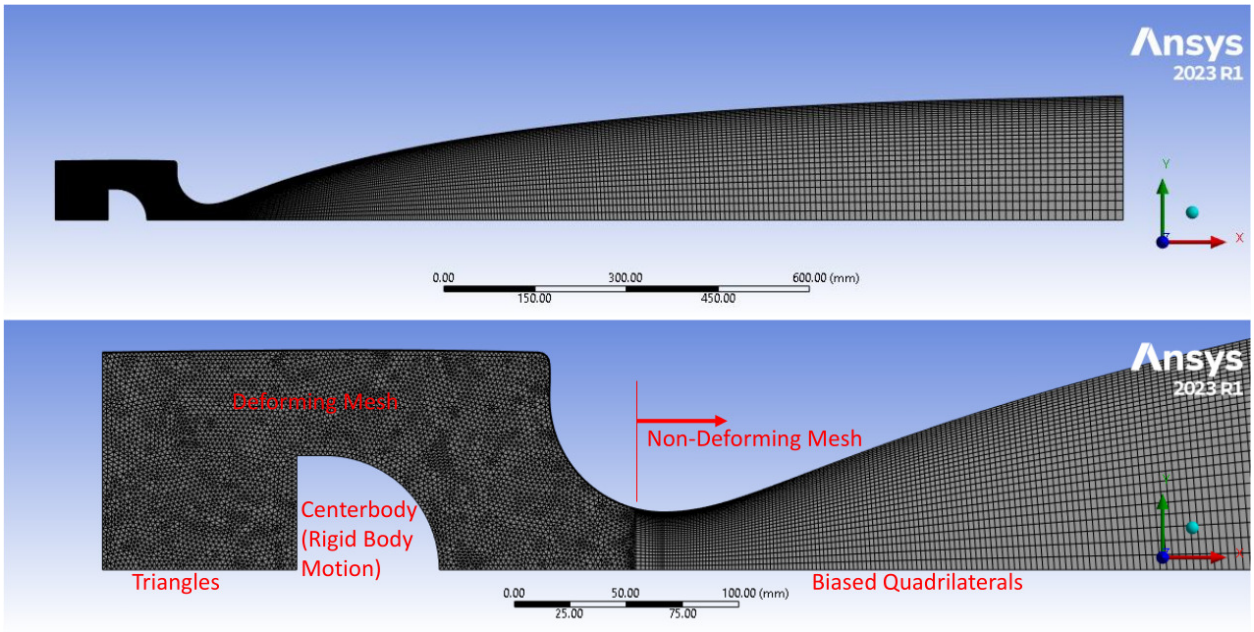

Fig. 8 Nozzle Mesh Setup.

The converging portion of the nozzle was designated as a laminar region, and the diverging section was modeled as a turbulent region via the k-ω shear stress transport (SST) turbulence model. The inlet was a pressure inlet with the conditions of Shot 367, the outlet was a pressure outlet, and the operating condition pressure was set to zero. The air

test gas was treated as an ideal gas, and viscosity was modeled via Sutherland's law.

Steady-state nozzle flow was used to initiate the dynamic simulation. Steady-state nozzle flow was first established via a transient, compressible flow simulation with a non-deforming mesh and the following flow variable initialization. The converging section was initialized via "standard initialization" with reservoir conditions, and the diverging section was then initialized via ANSYS "patch" with freestream flow conditions. The solution was marched transiently for 1.76 ms. Then the data file was transferred to transient flow simulation with dynamic meshing and centerbody motion. The model was then marched at a timestep of 5×10^{-6} s until the centerbody approached within approximately 0.0125 m of the nozzle wall. Then the timestep was reduced to 1×10^{-6} s until the centerbody touched the nozzle wall.

Centerbody kinematics (displacement and velocity vs. time) are presented in Fig. 9. Exit Mach number profiles are shown in Fig. 10 at different timesteps. Animations of the Mach contours of the M6 nozzle centerbody simulation are shown in Appendix B in Figs. 12a-12e, Figs. 13a-13c. Throat Mach number profiles are shown in Fig. 14.

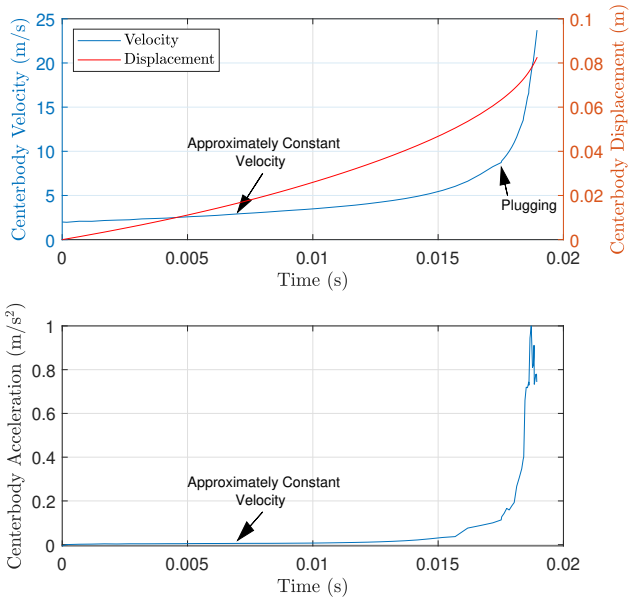

Fig. 9 Centerbody motion during ANSYS simulation of a sliding nozzle centerbody.

The CFD simulation of the nozzle centerbody revealed that the centerbody should be placed a considerable distance away from the nozzle converging section. When far from the nozzle converging wall, the centerbody has a negligible effect on nozzle operation and exit conditions, as shown by Fig. 10. The motion of the centerbody is characterized by three stages: (1) the impulse on the centerbody by the incident shock, (2) coasting of the centerbody towards the nozzle (at approximately constant velocity), and (3) suction of the centerbody by the nozzle flow. These stages are displayed in Fig. 9. In the region between the centerbody and the nozzle wall, jetting is observed in Figs. 13c and 14. The establishment of a secondary nozzle throat occurs in this region as the centerbody approaches close to the nozzle wall. The timestep (t = 0.019 s) captures this well in Fig. 14. Fig. 12e shows the collapse of the nozzle flow field as the centerbody plugs. Fig. 10 shows how the exit Mach Number profile changes with respect to time as the centerbody approaches its plugging position.

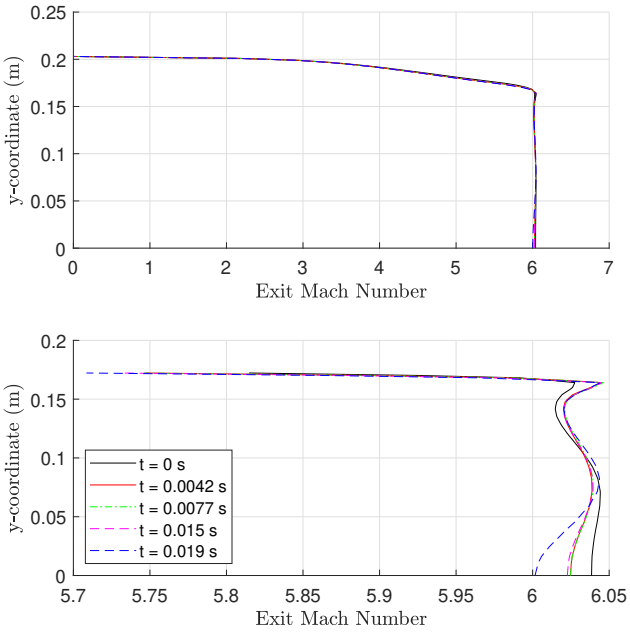

Fig. 10 Static Pressure Traces showing Plugging Times for Stevens Shock Tunnel using a sliding nozzle centerbody.

V. Conclusion

A preliminary set of experiments with a sliding nozzle centerbody is presented and compared with a previously debuted ball centerbody. The sliding centerbody allows for more predictable behavior: (1) by traveling along a prescribed linear path and (2) by having an adjustable mass to control the plugging time. An equation was derived and validated to calculate the approximate plugging time of the sliding centerbody. The sliding centerbody also is better at sealing the nozzle at the end of the test time, which saves driver gas and reduces facility recoil, especially for high-pressure helium-driven experiments (driver pressure $P_4 \geq 6.89$ MPa). Being able to control the inertia of the centerbody allows tunnel operators to prevent bouncing during high-pressure experiments. Further work includes measuring facility recoil with and without the centerbody, tuning the mass of the centerbody with respect to various run conditions, and improving the CFD simulation of the centerbody plugging motion to confirm reliable performance across all the operating regimes of the SST for the current M6 nozzle and future nozzles.

Appendix A: Shock Tunnel Pressure Traces

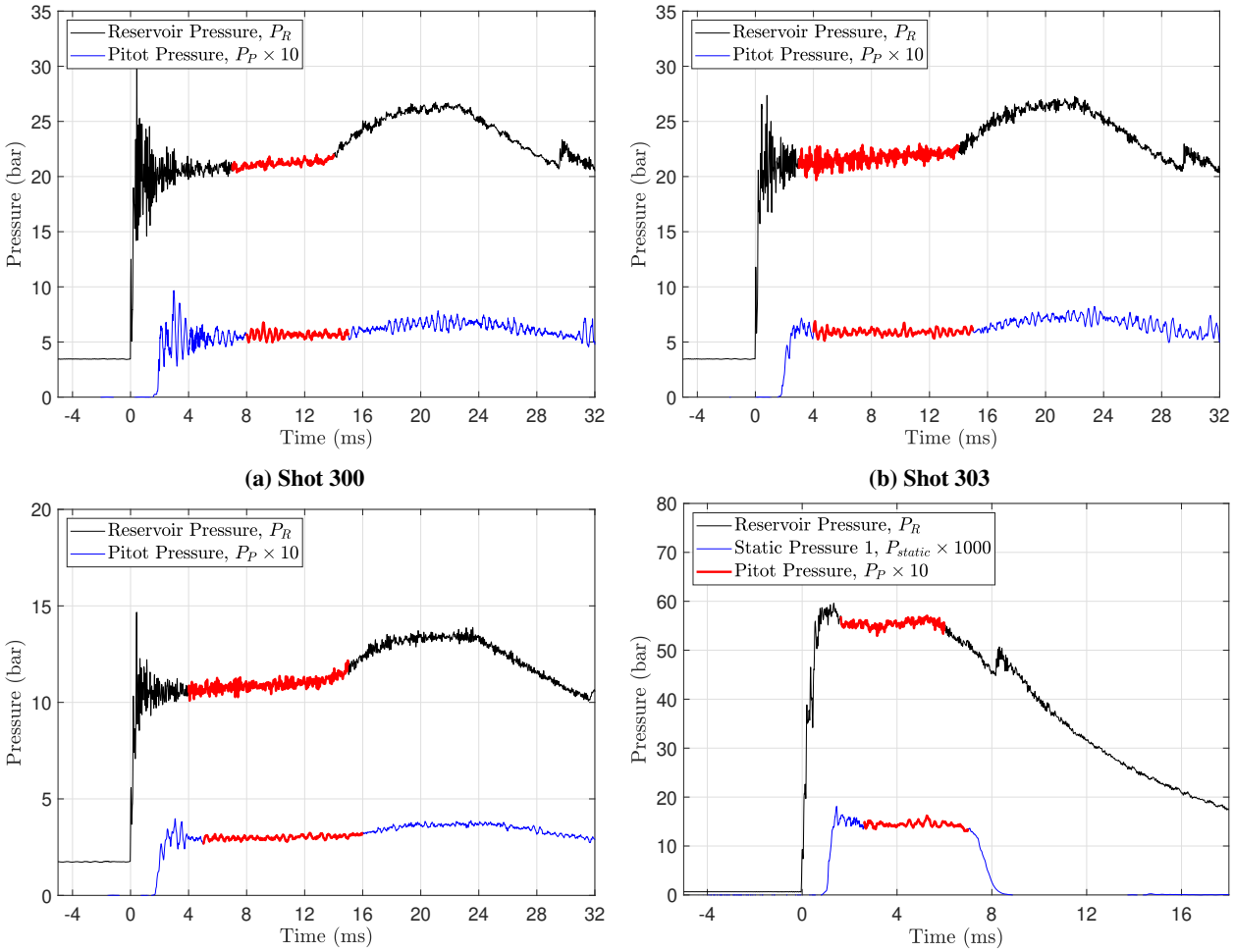

(a) Shot 300 **(b) Shot 303**

(c) Shot 306 **(d) Shot 391**

Fig. 11 Pressure Traces for Stevens Shock Tunnel Experiments with New Centerbody. Test times are indicated by a thick red line weight. Run conditions are listed in Table 1.

Appendix B: Additional Nozzle Simulation Results

This section includes animation snapshots of the dynamic ANSYS nozzle centerbody simulation.

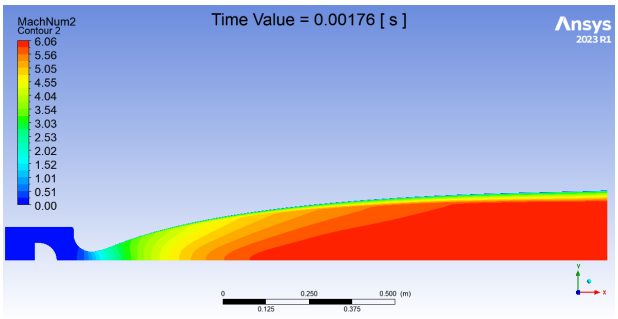

(a) $t = 0$ **s**

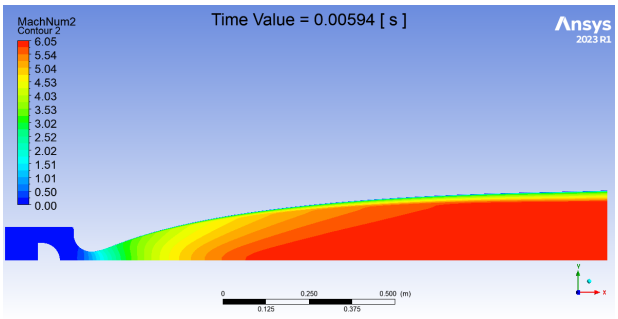

(b) $t = 0.0042$ **s**

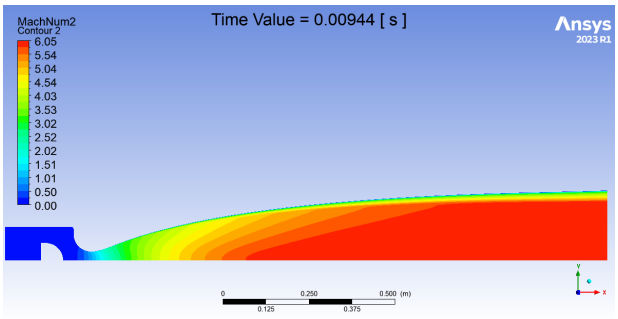

(c) $t = 0.0077$ **s**

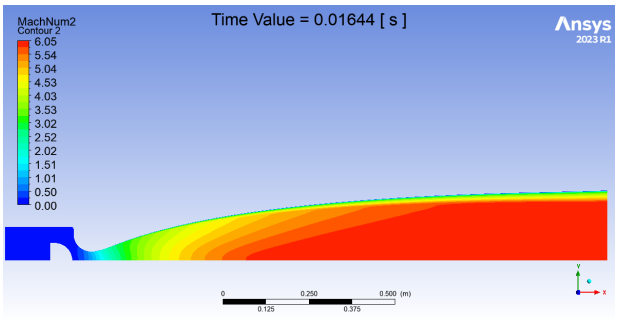

(d) $t = 0.015$ **s**

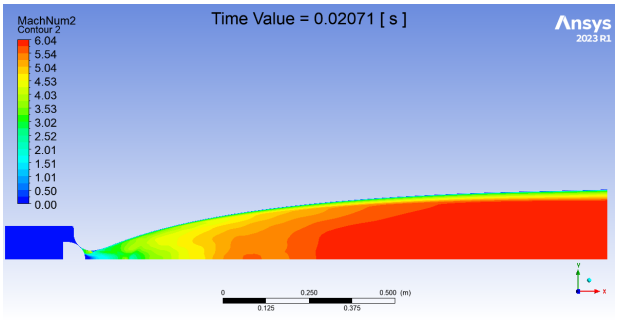

(e) $t = 0.019$ **s**

Fig. 12 Mach Contours for a He-driven Air Shot. Run conditions similar to those listed in Table 1.

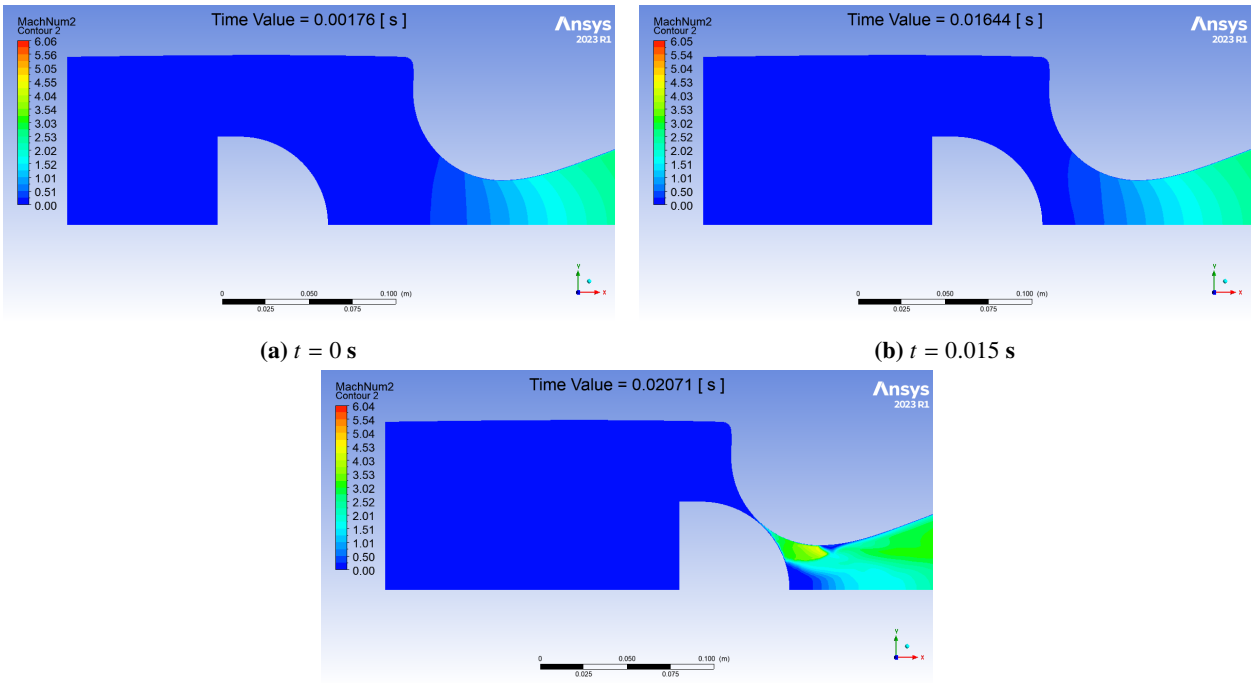

(a) $t = 0$ **s** **(b)** $t = 0.015$ **s**

(c) $t = 0.019$ **s**

Fig. 13 Closeup Mach Contours for a He-driven Air Shot. Run conditions similar to those listed in Table 1.

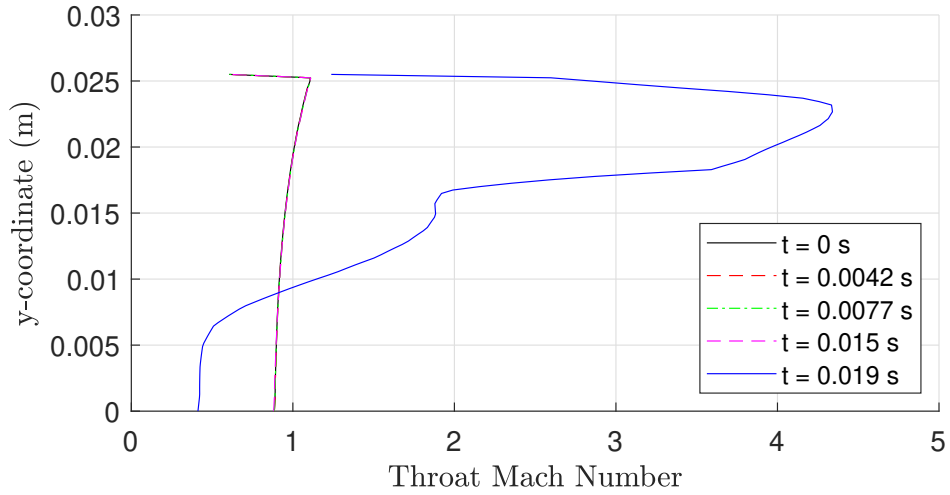

Fig. 14 Static Pressure Traces showing Plugging Times for Stevens Shock Tunnel using a sliding nozzle centerbody.

Acknowledgments

Ben A. Segall, David Shekhtman, Jett D. Langhorn, and Nicholaus J. Pariale were supported by ONR Grants, including N00014-20-1-2682, N00014-20-1-2637, N00014-23-1-2474. We thank Eric Marineau and the Office of Naval Research for sponsoring the construction and development of the Stevens Shock Tunnel. We also thank Ahsan Hameed, James H. Chen and Jason G. Cakerri for their assistance in running the Stevens Shock Tunnel.

References

[1] Holden, M. S., Wadhams, T. P., and MacLean, M. G., "Measurements in Regions of Shock Wave/Turbulent Boundary Layer Interaction from Mach 4 to 10 at Flight Duplicated Velocities to Evaluate and Improve the Models of Turbulence in CFD Codes," Tech. rep., CUBRC, 2014.

[2] Jewell, J. S., Parziale, N. J., Leyva, I. A., and Shepherd, J. E., "Effects of Shock-Tube Cleanliness on Hypersonic Boundary Layer Transition at High Enthalpy," *AIAA Journal*, Vol. 55, No. 1, 2017, pp. 332–338. https://doi.org/10.2514/1.J054897.

[3] Hertzberg, A., Wittliff, C. E., and Hall, J. G., "Summary of shock tunnel development and its application to hypersonic research," Tech. rep., 1961. AFOSR TR 60-139, AD0260731.

[4] Chue, R. S. M., and Eitelberg, G., "Studies of the transient flows in high enthalpy shock tunnels," *Experiments in Fluids*, Vol. 25, 1998, pp. 474–486. https://doi.org/10.1007/s003480050253.

[5] Hanneman, K., and Beck, W. H., "Aerothermodynamics Research in the DLR High Enthalpy Shock Tunnel HEG," *Advanced Hypersonic Test Facilities*, American Institute of Aeronautics and Astronautics, 2002, pp. 205–238. https://doi.org/10.2514/5.9781600866678.0205.0237.

[6] Holden, M. S., "Development and Code Evaluation Studies in Hypervelocity Flows in the LENS Facility," *Proceedings of the 2nd European Symposium on Aerodynamics for Space Vehicles*, European Space Agency, ESTEC, Noordwijk, The Netherlands, 1994, pp. 319–334.

[7] Holden, M. S., and Parker, R. A., "LENS Hypervelocity Tunnels and Application to Vehicle Testing at Duplicated Flight Conditions," *Advanced Hypersonic Test Facilities*, American Institute of Aeronautics and Astronautics, 2002, pp. 73–110. https://doi.org/10.2514/5.9781600866678.0073.0110.

[8] Lee, J. K., Park, C., and Kwon, O. J., "Experimental Study of Shock Tunnel Flow with a Stationary Throat Plug," *Shock Waves*, Vol. 22, 2012, pp. 295–305. https://doi.org/{10.1007/s00193-012-0370-2}.

[9] Lee, J. K., Park, C., and Kwon, O. J., "Experimental and Numerical Study of Stationary Throat Plug in Shock Tunnel," *Journal of Thermophysics and Heat Transfer*, Vol. 29, No. 3, 2015, pp. 482–495. https://doi.org/10.2514/1.T4084.

[10] Lee, J. K., Park, C., and Kwon, O. J., "Experimental Study of Moving Throat Plug in a Shock Tunnel," *Shock Waves*, Vol. 25, 2015, pp. 431–442. https://doi.org/{10.1007/s00193-015-0573-4}.

[11] Hornung, H. G., and Parziale, N. J., "Reflected Shock Tunnel Noise Control," *Proceedings of the 15th International Conference on the Methods of Aerophysical Research*, Akademgorodok, Novosibirsk Russia, 2010.

[12] Hornung, H. G., "Performance Data of the New Free-Piston Shock Tunnel at GALCIT," *Proceedings of 17th AIAA Aerospace Ground Testing Conference*, AIAA 1992-3943, Nashville, TN, 1992. https://doi.org/10.2514/6.1992-3943.

[13] Shekhtman, D., Hameed, A., Segall, B. A., Dworzanczyk, A. R., and Parziale, N. J., "Initial Shakedown Testing of the Stevens Shock Tunnel," *Proceedings of AIAA SciTech 2022*, AIAA 2022-1402, San Diego, California and Virtual Event, 2022. https://doi.org/10.2514/6.2022-1402.

[14] Segall, B. A., Shekhtman, D., Hameed, A., Chen, J. H., Dworzanczyk, A. R., and Parziale, N. J., "Debris Blocker and Flow Terminator for a Shock Tunnel," *AIAA Journal*, Vol. 61, No. 6, 2023, pp. 2739–2743. https://doi.org/10.2514/1.J062348.

[15] Segall, B. A., Shekhtman, D., Hameed, A., Chen, J. H., and Parziale, N. J., "Tagging Velocimetry in the Stevens Shock Tunnel," *Proceedings of AIAA Scitech 2023*, AIAA 2023-2337, National Harbor, Maryland and Virtual Event, 2023. https://doi.org/10.2514/6.2023-2337.

[16] Segall, B. A., Shekhtman, D., Hameed, A., Chen, J. H., and Parziale, N. J., "Profiles of streamwise velocity and fluctuations in a hypersonic turbulent boundary layer using acetone tagging velocimetry," *Experiments in Fluids*, Vol. 64, No. 122, 2023. https://doi.org/10.1007/s00348-023-03647-2.

[17] ASME, *B16.5-2009 Pipe Flanges and Flanged Fittings: NPS 1/2 Through NPS 24 Metric/Inch Standard*, ASME, 2009.

[18] ASME, *B31.1-2014 Power Piping: ASME Code for Pressure Piping, B31*, ASME, 2014.

[19] Mustafa, M. A., Parziale, N. J., Smith, M. S., and Marineau, E. C., "Nonintrusive Freestream Velocity Measurement in a Large-Scale Hypersonic Wind Tunnel," *AIAA Journal*, Vol. 55, No. 10, 2017, pp. 3611–3616. https://doi.org/10.2514/1.J056177.

[20] Korte, J. J., Lafferty, J. F., Smith, M. S., Lewis, D. R., Butcher, C. W., Fredrick, N. J., Zarzecki, M., and Tatum, K. E., "Determination of Hypervelocity Freestream Conditions for a Vibrationally Frozen Nitrogen Flow," *Proceedings of AIAA SciTech 2021*, AIAA-2021-0981, Virtual Event, 2021. https://doi.org/10.2514/6.2021-0981.

[21] Browne, S. T., Ziegler, J. L., and Shepherd, J. E., "Numerical Solution Methods for Shock and Detonation Jump Conditions," GALCIT - FM2006-006, Caltech, 2006.

[22] Gordon, S., and McBride, B., "Thermodynamic Data to 20000 K for Monatomic Gases," NASA TP-1999-208523, 1999.

[23] McBride, B. J., Zehe, M. J., and Gordon, S., "NASA Glenn Coefficients for Calculating Thermodynamic Properties of Individual Species," NASA TP-2002-211556, 2002.

[24] Hameed, A., Mustafa, M. A., Shekhtman, D., and Parziale, N. J., "Optimization of an Axisymmetric Mach 6 Reflected-Shock Tunnel Nozzle at Flight Enthalpy," *Proceedings of AIAA SciTech 2021*, AIAA-2021-0386, Virtual Event, 2021. https://doi.org/10.2514/6.2021-0386.